Magnetic Resonance in Medicine 64:138–148 (2010)

Tensor Kernels for Simultaneous Fiber Model Estimation and Tractography

Yogesh Rathi,[1]* James G. Malcolm,[1] Oleg Michailovich,[2] Carl-Fredrik Westin,[3]
Martha E. Shenton,[1,4] and Sylvain Bouix[1]

This paper proposes a novel framework for joint orientation distribution function estimation and tractography based on a new class of tensor kernels. Existing techniques estimate the local fiber orientation at each voxel independently so there is no running knowledge of confidence in the measured signal or estimated fiber orientation. In this work, fiber tracking is formulated as recursive estimation: at each step of tracing the fiber, the current estimate of the orientation distribution function is guided by the previous. To do this, second-and higher-order tensor-based kernels are employed. A weighted mixture of these tensor kernels is used for representing crossing and branching fiber structures. While tracing a fiber, the parameters of the mixture model are estimated based on the orientation distribution function at that location and a smoothness term that penalizes deviation from the previous estimate along the fiber direction. This ensures smooth estimation along the direction of propagation of the fiber.

In synthetic experiments, using a mixture of two and three components it is shown that this approach improves the angular resolution at crossings. In vivo experiments using two and three components examine the corpus callosum and corticospinal tract and confirm the ability to trace through regions known to contain such crossing and branching. Magn Reson Med 64:138–148, 2010. © 2009 Wiley-Liss, Inc.

Key words: diffusion-weighted MRI; tractography; diffusion tensor estimation; high order tensors; spherical harmonics

The advent of diffusion-weighted MRI has provided the opportunity for noninvasive investigation of neural architecture. Using this imaging technique, clinicians and neuroscientists want to ask how neurons originating from one region connect to other regions or how well defined those connections may be. For such studies, the quality of the results relies heavily on the chosen fiber representation and the method of reconstructing pathways.

To begin studying the microstructure of fibers, we need a model to interpret the diffusion-weighted signal. Such models fall broadly into two categories: parametric and nonparametric. One of the simplest parametric models is the diffusion tensor, which describes a gaussian estimate of the diffusion orientation and strength at each voxel (1,2). While robust, this model can be inadequate in cases of mixed fiber presence or more complex orientations (3,4). To handle more complex diffusion patterns, various parametric models have been introduced: weighted mixtures (5–8), higher-order tensors (9,10) and directional functions (11–13).

Nonparametric models often provide more information about the diffusion pattern. Instead of estimating a discrete number of fibers as in parametric models, nonparametric techniques estimate an orientation distribution function (ODF) describing an arbitrary configuration of fibers. For this estimation, Tuch (14) introduced Q-ball imaging to numerically compute the ODF (also refered to as diffusion-ODF[dODF]) using the Funk-Radon transform. The use of spherical harmonics (SH) simplified the computation with an analytic form (15–17). A good review of both parametric and nonparametric models can be found (18,19).

Deterministic tractography involves directly following the diffusion pathways. In the single-tensor model, this means simply following the principal diffusion direction (20), while multifiber models often include techniques for determining the number of fibers present or when pathways branch (7,21). Since the estimated model at each location is inherently noisy, some methods perform path regularization using a filtering technique (22).

In order to perform deterministic tractography using nonparametric methods, one has to use a separate algorithm to find the dODF maxima. Since the dODF peaks are very smooth, the principal diffusion direction obtained from it is very noisy (19). Recent work has focused on estimating the fiber-ODF (fODF) either directly from the signal or from the dODF (23–25). For example, Bloy and Verma (25) found them as maxima on the surface of a high-order tensor and Schultz and Seidel (26) decompose a high-order tensor into a mixture of rank-1 tensors. Ramirez et al. (27) provide a quantitative comparison of several such techniques.

Another popular technique to estimate the fODF has been to use spherical deconvolution (12,28–32). In this approach, a model for the signal response of a single fiber is assumed and the observed signal is deconvolved to obtain the true fODF. This technique sharpens the peak of the ODF and it becomes much easier to extract the maxima. Descoteaux et al. (19) have shown improvement in tractography results, with fODF computed using spherical deconvolution.

An alternative method is to use a mixture model of directional kernels, each representing a single fiber response. The advantages of the mixture model are that a separate algorithm is not needed to find the fODF maxima since

---

[1] Psychiatry Neuroimaging Laboratory, Brigham and Women's Hospital, Harvard Medical School, Boston, Massachusetts, USA

[2] Department of Electrical Engineering, University of Waterloo, Canada

[3] Laboratory for Mathematical Imaging, Brigham and Women's Hospital, Harvard Medical School, Boston, Massachusetts, USA

[4] VA Boston Healthcare System, Brockton Division, Brockton, Massachusetts, USA

*Correspondence to: Yogesh Rathi, Ph.D., Psychiatry Neuroimaging Laboratory, Brigham and Women's Hospital, Harvard Medical School, 1249 Boylston St, Boston, MA 02215. E-mail: yogesh@bwh.harvard.edu

Received 6 April 2009; revised 30 June 2009; accepted 21 October 2009.
DOI 10.1002/mrm.22292

the kernel parameters include the principal diffusion direction. Further, the scaling parameter can adjust the shape of the ODF, i.e., it can adjust the single fiber response based on the observed data (white matter, gray matter, cerebrospinal fluid, etc.) and hence allows for better model fit for white matter and gray matter regions. The disadvantage, however, is that the number of fibers (components of mixture model) at each location have to be kept fixed or determined online during estimation.

MATERIALS AND METHODS

In this work, we first propose a novel kernel based on second-and higher-order rank-1 tensors. The two parameters of the kernel determine the orientation and shape (scaling) of the kernel. We will use this tensor kernel to represent fODF.

Second, while most of the approaches listed above perform dODF (or fODF) estimation independently at each voxel, we describe in this paper a method to estimate the model parameters and perform tractography simultaneously as we trace a fiber from its seed to termination. In this way, the estimation at each position builds upon the previous estimates along the fiber.

We use a mixture of two/three components and formulate our cost function in such a way that if there is one fiber, the components of the mixture align in the same general direction and disperse if there is more than one fiber at a given location. Further, we constrain the solution to be consistent with the model estimated at the previous location.

Using causal estimation in this way yields inherent path regularization and accurate fiber resolution at crossing angles not found with independent optimization.

APPROACH

In this section, we propose a function using second- and higher-order tensors capable of representing ODFs and examine some of their properties. We also define two different cost functions, which are minimized in order to estimate the parameters of the mixture model.

Tensor Kernel

One of the goals of this paper is to extract the fODF from the dODF. To do this, we need kernels (functions) that can accurately represent a fODF. Second- and higher-order tensors provide a way to represent functions on the sphere (the fODF is a function on the sphere). In this work, we treat order-l tensors $\mathbb{T}$ in a given orthonormal Cartesian coordinate system as quantities whose elements are addressed by l indices. The employed tensors are supersymmetric, i.e., their elements $\mathbb{T}_{i_1 i_2 \ldots i_l}$ are invariant under arbitrary permutations of indices $i_1 i_2 \ldots i_l$. A function $D(\mathbf{g})$ on the unit sphere is given by its induced homogeneous form. For an order-l tensor $\mathbb{T}$ in three dimensions, it reads:

$$D(\mathbf{g}) = \sum_{i_1=1}^{3}\sum_{i_2=1}^{3} \ldots . \sum_{i_l=1}^{3} \mathbb{T}_{i_1 i_2 \ldots i_l} g_{i_1} g_{i_2} \cdots g_{i_l}$$

The above equation can be compactly written using the tensor contraction operator "**:**"

$$D(\mathbf{g}) = \mathbb{T} : \mathbb{G}^l,\ \mathbb{G}^l = \underbrace{\mathbf{g} \otimes \mathbf{g} \otimes \ldots \mathbf{g}}_{l\ times}, \quad \mathbf{g} = [g_1\ g_2\ g_3]^T, \qquad [1]$$

where $\otimes$ is the outer product operation and $\mathbb{G}^l$ is a rank-1 tensor of order-l. The tensor contraction operator **:** is an inner product between matrices analogous to an inner product between vectors.

Let $\mathbf{g}_1 \mathbf{g}_2 \ldots \mathbf{g}_n \in \mathcal{S}^3$ be the directions that represent a uniform sampling of the sphere. Then, we propose to use the following tensor kernel to represent an ODF with principal diffusion direction along $\mathbf{t}$:

$$D(\mathbf{g}_i) = \left(\mathbb{T}^l : \mathbb{G}_i^l\right)^p, \qquad [2]$$

where $\mathbb{T}^l$ is the order-l tensor of rank-1 in direction $\mathbf{t}$, $\mathbb{G}_i^l$ is order-l tensor in direction $\mathbf{g}_i$, and p is a scaling parameter. Note that a particular case of this function has been used in the literature with $p = 1$ (26,33). This is, however, the first time we have modified it to have a scaling parameter, giving more flexibility to represent various kinds of shapes. Figure 1 shows the effect of the scaling parameter p on the shape of the function. The top row shows the function for order-*6*, middle for order-*4* and bottom for order-*2*. Thus, we have a family of functions, given by their order, that can represent single-fiber response. The higher-order kernels differ from their lower-order counterparts in terms of the scaling. Note that we only require three parameters that can uniquely define the tensor kernel: the principal diffusion direction $\mathbf{t}$ requires two parameters in spherical coordinates and one scaling parameter p.

Mixture Model

In diffusion-weighted imaging, image contrast is related to the strength of water diffusion, and our goal is to accurately relate these signals to an underlying model of fiber orientation. At each image voxel, diffusion is measured along a set of distinct gradients, $\mathbf{g}_1, \ldots, \mathbf{g}_n \in \mathcal{S}^3$ (on the unit sphere), producing the corresponding signal, $S = [s_1, \ldots, s_n]^T \in \mathcal{R}^n$. Thus, the signal S is a function defined on the sphere.

A popular method to represent functions on the sphere is using spherical harmonics (SH) (15–17). Given any band-limited signal S defined on the sphere, one can write it as an expansion in terms of the SH basis as: $S(\theta, \phi) = \sum_{l=0}^{L} \sum_{m=-l}^{l} c_{l,m} Y_{l,m}$, for any direction (θ, ϕ), where $Y_{l,m}$ are the basis functions given by:

$$Y_{l,m}(\theta, \phi) = \sqrt{\frac{(2l+1)(l-m)!}{4\pi(l+m)!}} P_{l,m}(\cos\theta) e^{im\phi},$$

and $P_{l,m}$ is the associated Legendre polynomial. The above equations can be written as a linear system of equations and $c_{l,m}$ can be computed using the Moore-Penrose pseudoinverse. To make the method robust to noise, Descoteaux et al. (17) proposed a regularized version by adding a smoothness constraint.

Once the signal representation is obtained in the SH basis, the corresponding dODF can be analytically computed using the Funk-Radon transform (17). This method

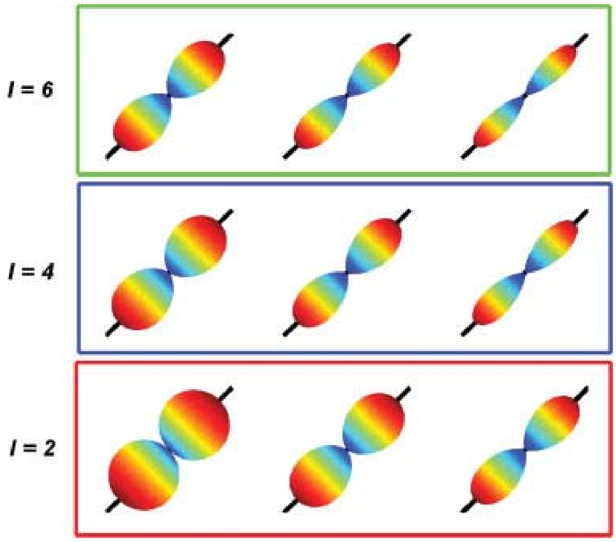

FIG. 1. Tensor kernels of different orders and scales. Top row: order-6; middle: order-4; and bottom: order-2. Left to right: $P = 0.5, 1, 2$. Red to blue shows higher to lower diffusion values. [Color figure can be viewed in the online issue, which is available at www.interscience.wiley.com.]

is very fast and robust to noise. In the remainder of this work, we will assume that the dODF has been precomputed using SH (see (17) for details). There has been a lot of work recently to extract the fODF from dODF using spherical deconvolution (12,28–30,32). This method assumes a fixed single-fiber response while allowing for variable numbers of fibers to be estimated.

In this work, we seek to estimate the fODF using a different strategy by allowing for variation in single-fiber response but keeping the number of fibers fixed. This can be done by fitting the dODF using a mixture of tensor kernels. While one can assume a mixture of any number of components, we choose to start with a mixture involving two and three weighted tensor kernels. While the work of Behrens et al. (34) showed that at a b-value of 1000 the maximum number of detectable fibers is two, several other studies restricted their analysis to two-fiber models due to problems with estimating more than two components (6,7,23). In this work, we perform experiments on synthetic data using two components and later show an extension to three components. Similar results are shown for in vivo data.

The model we intend to use in this study is given by:

$$D(\mathbf{g}_i) = \sum_{j=1}^{N} w_j \left(\mathbb{T}_j^l : \mathbb{G}_i^l\right)^{p_j}, \qquad [3]$$

where $D(\mathbf{g}_i)$ is the dODF in direction $\mathbf{g}_i$, w_j are the respective weights of the components, $\mathbb{G}_i^l$ is the lth order rank-1 tensor obtained from the gradient direction $\mathbf{g}_i$, and $\mathbb{T}_j^l$ is lth order rank-1 tensor with principal diffusion direction $\mathbf{t}_j$. N is the total number of components used in the mixture, which in our case could be two or three. Thus, a two-component dODF can be uniquely represented using 10 parameters (if $\mathbf{t}_j \in \mathcal{R}^3$) or eight parameters if the directions are represented in spherical coordinates. We should also clarify that D is the dODF but the individual components of the mixture model give the fODF in direction $\mathbf{t}_j$. The remainder of this section will focus on estimating the free parameters of this mixture model, i.e., $\{\mathbf{t}_j, w_j, p_j, \}_{j=1}^N$.

Independent Estimation

Given the scanner signal $S \in \mathcal{R}^n$, we compute the corresponding dODF $F = [F_1, F_2, \ldots F_n] \in \mathcal{R}^n$ using SH (17) and min-max normalize it (14). One can now minimize the following cost function to estimate the parameters:

$$\tilde{E} = \sum_{i=1}^{n} (F_i - D_i)^2 = \sum_{i=1}^{n} \left(F_i - \sum_{j=1}^{N} \hat{w}_j \left(\mathbb{T}_j^l : \mathbb{G}_i^l\right)^{\hat{p}_j} \right)^2, \qquad [4]$$

where we have used the shorthand notation $D(\mathbf{g}_i) = D_i$ and $F(\mathbf{g}_i) = F_i$. Equation 4 can be minimized using the Levenberg-Marquardt nonlinear optimizer. However, the minimum could be a degenerate solution with negative $\hat{w}_j$ and/or $\hat{p}_j$. To overcome this problem, we use the exponential map to guarantee positivity of the weight and scaling parameters (10), i.e., we use $w_j = \exp(-\hat{w}_j)$ and $p_j = \exp(\hat{p}_j)$ in Eq. 4:

$$\tilde{E} = \sum_{i=1}^{n} \left(F_i - \sum_{j=1}^{N} w_j \left(\mathbb{T}_j^l : \mathbb{G}_i^l\right)^{p_j} \right)^2. \qquad [5]$$

To obtain volume fraction contribution for each component, one can normalize the weights so that they sum to 1. Figure 2 shows how the individual fODFs combine to give the observed dODF. Note that maxima of F would not have revealed the individual fiber composition of the dODF.

Given the signal at each location in the brain, one could independently estimate the dODF and the mixture model parameters, as is done in most of the techniques presented in the literature. However, in this paper, we make the observation that the diffusion of water molecules is not independent and is highly correlated along the direction of the fiber bundle. We will demonstrate that taking this into account significantly improves tractography results.

Smooth Estimation and Tractography

In this work, we take this spatial correlation into account and propose to do simultaneous model estimation and tractography. This means we recursively estimate the model

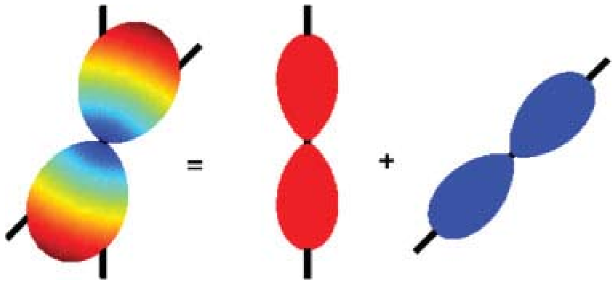

FIG. 2. Mixture components of dODF at an angle of 45° [Color figure can be viewed in the online issue, which is available at www.interscience.wiley.com.]

parameters at location x based on the observed dODF at x and the model parameters estimated at $x-1$ (previous location along the fiber tract). Once the model parameters are estimated, we propagate a unit step along the most consistent direction. Causal estimation and tracking in this way allow for smooth and accurate estimation of the fiber.

In order to take into account the estimated model parameters at the previous location $x-1$, we modify the cost function in Eq. 5:

$$E(x)=\sum_{i=1}^{n}\left(F_i(x)-\sum_{j=1}^{N}w_j\left(\mathbb{T}_j^l(x):\mathbb{G}_i^l\right)^{p_j}\right)^2 + \lambda_1\sum_{j=1}^{N}(w_j(x)-w_j(x-1))^2+\lambda_2\sum_{j=1}^{N}(p_j(x)-p_j(x-1))^2 + \lambda_3\sum_{j=1}^{N}\left(1-\left(\mathbf{t}_j(x)^T\mathbf{t}_j(x-1)\right)^2\right), \quad [6]$$

where the first is the data consistency term at location x, and the 2^{nd}, 3^{rd} and 4^{th} terms ensure that the weights, scale, and direction are consistent with the previous estimation at $x-1$. The constants $\lambda_1, \lambda_2, \lambda_3$ are user-defined constants that determine the influence of the previous estimate on the current. In our experiments, we empirically obtained these constants by choosing the ones that gave the best tractography results on synthetic data. One could, however, use a strategy that either does a brute force search or minimizes the error to obtain these constants. We, however, noticed that the estimation works well for a braod range of values. Eq. 6 can be minimized using an Levenberg-Marquardt optimizer.

To perform tractography, we repeatedly minimize Eq. 6 at each voxel location x and then propagate a unit step in the most consistent direction. The principal diffusion directions are given by $\mathbf{t}_1$ and $\mathbf{t}_2$, and hence there is no need for a separate peak-finding algorithm. Smooth parameter estimation along the fiber in this way gives significantly better results than independent estimation, as is clear from synthetic and in vivo results given in the next section. A summary of the entire algorithm is given below:

1. Compute the dODF using SH (17).
2. Min-max normalize the dODF to obtain $F(x)$
3. Minimize Eq. 6 using a Levenberg-Marquardt optimizer to obtain $\{\mathbf{t}_j, w_j, p_j\}_{j=1}^{N}$.
4. Move a unit step that is consistent with the incoming direction, i.e., move a step along $\mathbf{t}_1(x)$.
5. Stop if the generalized fractional anisotropy (14) is less than 0.05 or if the radius of curvature of the fiber at location x is less than 0.87 or the weight of the component in the direction of propagation is less than 40% of the other weight.
6. Otherwise go to step 1 and repeat for position $x+1$.

Before we conclude this section, we note some existing techniques that do spatial regularization during estimation (35,36). In Fillard et al. (35), the authors estimate a single tensor using the log-Euclidean metric, along with a spatial smoothness term. In Assemlal et al. (36), the authors extend it for smooth estimation of the spherical harmonic coefficients. Both of these methods assume a spatial neighborhood ($3 \times 3 \times 3$) within which the regularization is done. However, none of these methods perform simultaneous tractography and estimation in their framework (as is proposed in this work).

We also note some techniques that have used mixture model to represent ODFs. In recently proposed work (26), the authors use a tensor decomposition approach to find a mixture of rank-1 tensors of order-l that best fit the given dODF. Some of the important differences with this method are as follows: (a) The authors estimate the standard high-order tensor of rank-1 with a single fixed scale ($p = 1$). In order to compensate for the scaling, they deconvolve the dODF using a fixed kernel and map it to an appropriate space so that a rank-1 order-l tensor can be fit to it. (b) Once again, the authors perform an independent estimation at each voxel location and then do tractography on it. McGraw et al. (11) use a mixture model of von-Mises Fisher function to estimate an ODF. They also perform independent estimation at each voxel and thus ignore the correlation in fiber geometry. Sotiropoulos et al. (37) estimate the parameters of a two-tensor gaussian mixture model using relaxation labeling as their regularizer.

RESULTS

We first use experiments with synthetic data to validate our technique against ground truth. We confirm that our approach reliably recognizes crossing fibers over a broad range of angles. Comparing against two alternative multi-fiber optimization techniques, we find that the constrained tractography approach gives consistently superior results. Next, we perform tractography through crossing fiber fields and qualitatively examine the underlying orientations and branchings (see Section Synthetic Tractography). Last, we examine a real dataset to demonstrate how constrained estimation is able to pick up fibers and branchings known to exist in vivo yet that are undetectable using deconvolved SH and single tensor models (see Section In Vivo Tractography).

Following the experimental method of generating synthetic data (19,26,30), we pull from our real data set the 300 voxels with highest fractional anisotropy and compute the average eigenvalues among these voxels: $\{1200, 100, 100\}\mu\text{m}^2/\text{msec}$ (fractional anisotropy $= 0.91$). We generated synthetic MR signals according to a gaussian mixture model, as done in Tuch (14), using these eigenvalues to form an anisotropic tensor at both $b = 1000$ and $b = 3000$, with 81 gradient directions uniformly spread on the hemisphere. We generate two separate data sets, each with a different level of Rician noise along the fiber direction: low noise (signal-to-noise ratio (SNR) $\approx$ 10 dB) and high noise (SNR $\approx$ 5 dB).

Throughout the experiments, we draw comparison to two other independent optimization techniques. In what follows, we use the second- and fourth- order tensor kernels. First, we use the proposed tensor kernel within the mixture model framework but do an independent optimization using Eq. 5. Second, we use SH for modeling (30) and fODF sharpening with peak detection, as described in Descoteaux et al. (19) (order $l = 6$, regularization $L = 0.006$). This provides a comparison with an independently estimated, model-free representation. Last, when

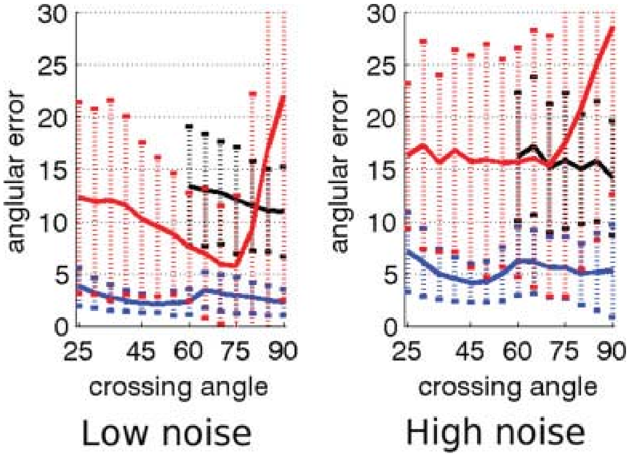

FIG. 3. Angular error for second-order kernel using constrained optimization (blue), independent optimization (red), and sharpened SH (black) for $b = 1000$. The dotted vertical bars show range of 1 standard deviation. Left: low noise; right: high noise. [Color figure can be viewed in the online issue, which is available at www.interscience.wiley.com.]

performing tractography on real data, we use single-tensor streamline tractography as a baseline, using the freely available Slicer 2.7 (http://www.slicer.org).

Angular Resolution

While the independent optimization techniques can be run on individually generated voxels, care must be taken in constructing reasonable scenarios to test the causal filter. For this purpose, we constructed an actual two-dimensional field through which to navigate (see Fig. 9). In the middle is one long fiber pathway where the tracker begins estimating a single tensor but then runs into a field of voxels with two crossed fibers at a fixed angle. We computed the angular error over this region using both sharpened SH and independent optimization (5). We generated several similar fields, each at a different fixed angle. By varying the size of the crossing region or the number of fibers run, we ensured that each technique performed estimation on at least 500 voxels.

We looked at the error in angular resolution by comparing the constrained approach to independent optimization and sharpened SH. For the tensor kernels (two components), we show comparison using both, second- and fourth- order tensors. Consistent with other results reported in (17,19), sharpened SH are generally unable to detect and resolve angles below 50° for $b = 1000$. Figures 3 and 4 confirm this.

As expected, the independent optimization technique also reports large errors since the Levenberg-Marquardt optimizer gets stuck in local minimum. For example, any dODF can be represented using a single component with significant weight and appropriate scaling parameter while rendering the contribution from the other component to zero by setting the weight to be zero. Such solutions contribute to large errors when using independent optimization.

However, in the constrained estimation technique, we constrain the weight and the scaling parameter to be close to its previous estimate, which results in a better estimation of the parameters. For in vivo and synthetic data, the user-defined values of $\lambda_1, \lambda_2, \lambda_3$ in Eq. 6 were emprirically found to be 2.5, 1, and 0.15, respectively, for a second-order tensor kernel. Thus, the deviation of the weights from the previous estimate had the largest penalty, the scaling parameter had a little more flexibility, and the penalty on direction parameter was still lower. Intuitively, for the case of a single fiber, this means that equally weighted, similarly aligned components are more preferable than a single component with the correct direction but zero contribution from the second component. Thus, upon encountering a region of dispersion, the second component is poised and ready to begin branching. Overall, the relative weighting of the penalty terms ensures that there is no abrupt change in either the weight or the scale of the estimated fODF along the fiber but still allows flexibility to capture fiber crossings at high angles.

This experiment demonstrates that for $b = 1000$, the constrained approach consistently resolves angles down to 25−30° with 5° error compared to independent optimization, which reports very high error for certain angles and sharpened SH, which fails to reliably resolve below 60° with as much as 15° error. For $b = 3000$, the constrained approach consistently resolves down to 20−30° with 1−2° error compared to sharpened SH which cannot resolve below 50° with 5° error (Fig. 5). Further, the angular errors reported using the constrained optimization with second- and fourth-order tensor kernels are very close, and hence we will only show in vivo results using the second-order tensor kernel.

We also performed a similar experiment to test how well our method performs in the case of three crossing fibers. In this case, we used a mixture of three components with different crossing angles, as described earlier. Figure 6 demonstrates that the proposed method has lower angular error than sharpened SH. Figure 7 shows orientation and weights of three components as they trace a fiber

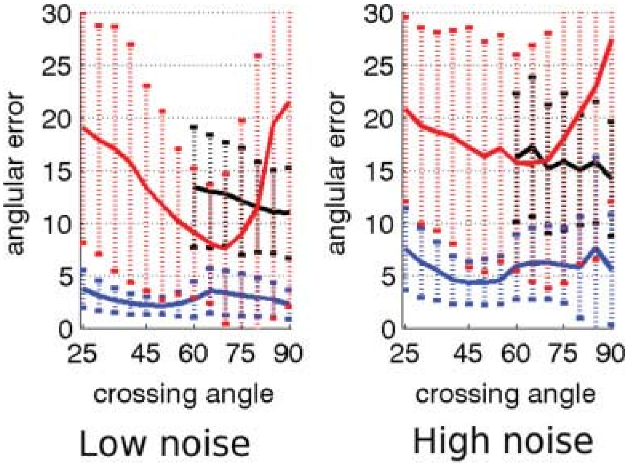

FIG. 4. Angular error for fourth-order kernel using constrained optimization (blue), independent optimization (red), and sharpened SH (black) for $b = 1000$. The dotted vertical bars show range of 1 standard deviation. Left: low noise; right: high noise. [Color figure can be viewed in the online issue, which is available at www.interscience.wiley.com.]

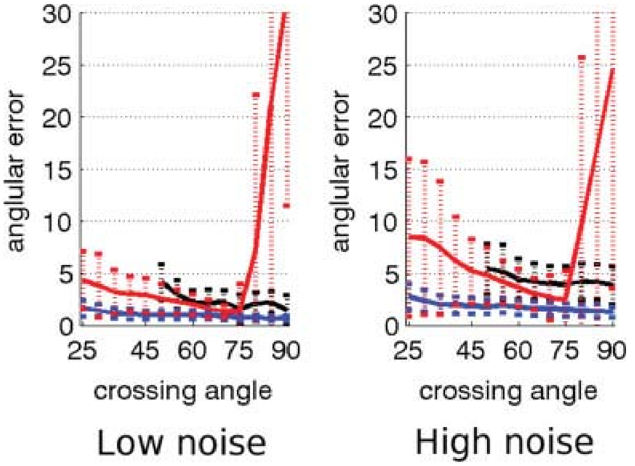

FIG. 5. Angular error for second-order kernel using constrained optimization (blue), independent optimization (red), and sharpened SH (black) for $b = 3000$. The dotted vertical bars show range of 1 standard deviation. Left: low noise; right: high noise. [Color figure can be viewed in the online issue, which is available at www.interscience.wiley.com.]

that passes through a fiber field with two crossing bundles. Notice that the weights are zero when there is only one component, while the weight for two components is nonzero in the region with twofibers and then falls back to single component being dominant once again, in accordance with the data. This demonstrates that the proposed method can adaptively change the weights, depending on the number of fibers present at each voxel.

Finally, Fig. 8 shows the precision of the proposed method in the presence of varying levels of noise. On the x-axis is the SNR ($\frac{\sigma_s}{\sigma_n}$), where σ_s and σ_n are the standard deviation of the signal and noise, respectively. Y-axis shows the average angular error for $b = 1000$ and $b = 3000$. We should note that the SNR reported is for the mean baseline image and that the actual SNR varies quite significantly in each gradient direction. Thus, an SNR of 20 for the baseline image could mean an SNR of 0.25 in the fiber direction and 35 in the direction orthogonal to it. This important fact should be kept in mind while inferring the results for Fig. 8.

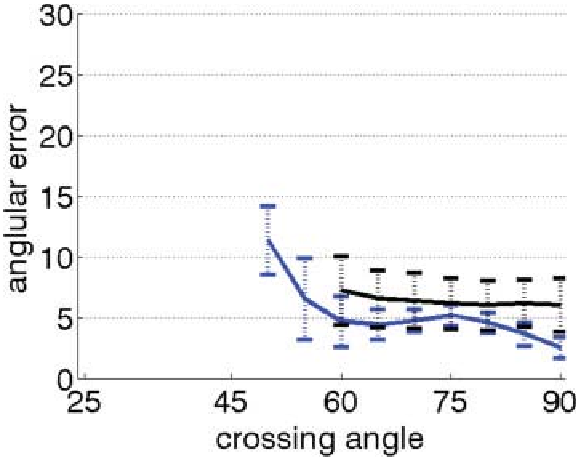

FIG. 6. Angular error for second-order kernel using constrained optimization (blue), and sharpened SH (black) for $b = 3000$ and three-component model with three fiber crossings (high noise). The dotted vertical bars show range of 1 standard deviation. [Color figure can be viewed in the online issue, which is available at www.interscience.wiley.com.]

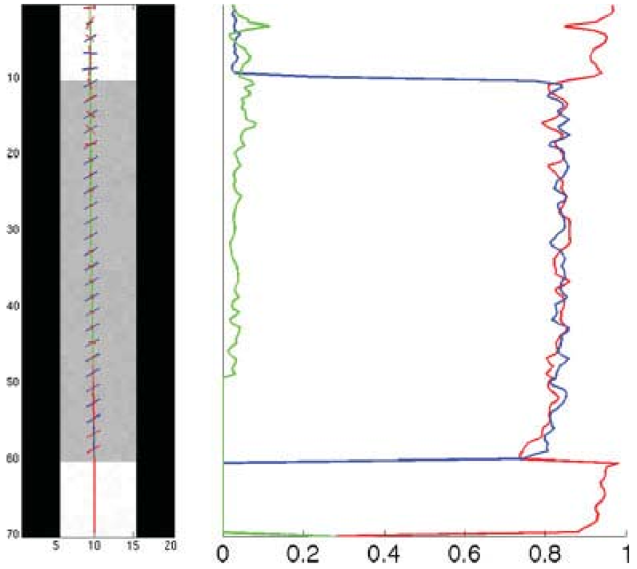

FIG. 7. Figure shows tracing a three-component model through a field of single and two tensors (crossing at 60°). The weights of each of the components are also shown, indicating that two of them are zero in the case in which a single fiber is present and only one of them is zero in the case in which two fibers are present. Note that since the weight of the third component is zero, its orientation is inconsequential. [Color figure can be viewed in the online issue, which is available at www.interscience.wiley.com.]

Synthetic Tractography

Having verified the technique's accuracy, we now turn to the resulting tractography. Figure 9 provides examples of synthetic crossing fiber fields, each at different fixed angles: 40°, 50°, 60° ($b = 3000$, high-noise). In our experiments, we

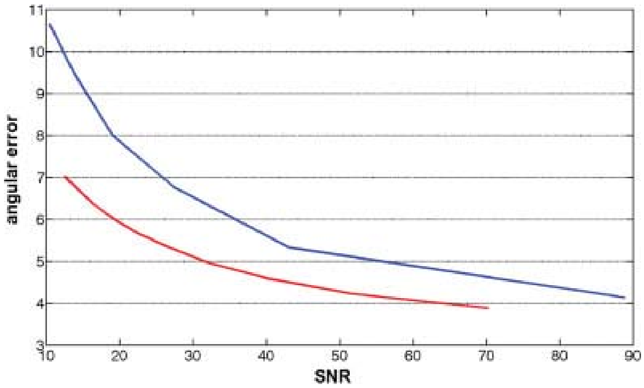

FIG. 8. The precision of the proposed method in the presence of varying levels of noise. X-axis is the SNR, while the y-axis is the angular error. Blue is for $b = 1000$, while red is for $b = 3000$. [Color figure can be viewed in the online issue, which is available at www.interscience.wiley.com.]

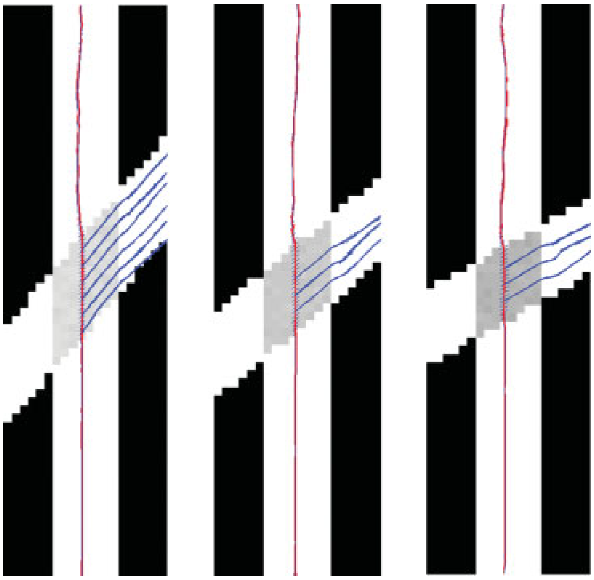

FIG. 9. Tracing a single fiber with other fibers intersecting at angles of 40°, 50°, and 60° (left to right) in the crossing region ($b = 3000$). Notice that the directions of the two components align when there is only one fiber, while the second component is picked up in the crossing region. [Color figure can be viewed in the online issue, which is available at www.interscience.wiley.com.]

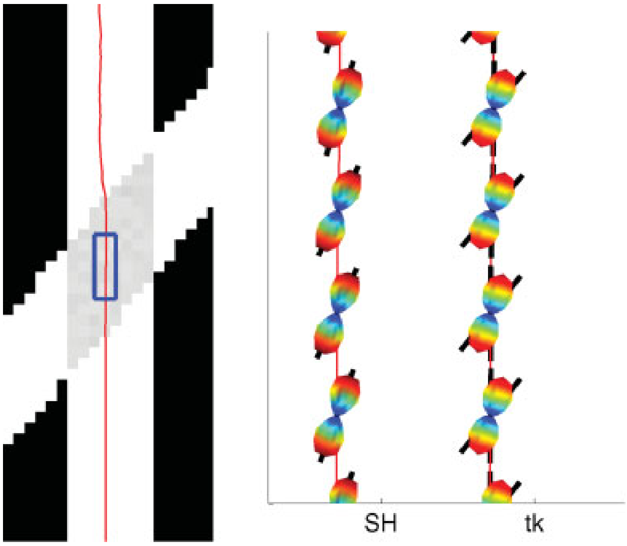

FIG. 10. Single-fiber tractography with the second component at 40° and $b = 3000$. Right: Estimated fODF using sharpened SH and constrained optimization using second-order tensor kernel (tk). Notice that SH is able to pick up only one component in the crossing region. [Color figure can be viewed in the online issue, which is available at www.interscience.wiley.com.]

start fibers from the bottom and propagate upward where they gradually encounter the crossing region. Here we show one such fiber and use blue glyphs to indicate the second component detected as it passes through the crossing region. In general, we found that in regions with only one true fiber present (those outside the crossing), the second component roughly aligned with the first.

The tractography was initialized by estimating the parameters in the seed region using a dictionary-based matching pursuit algorithm (38). In our implementation, we simply project against a dictionary populated with two tensor-kernel components at various P values and equal weights. While our signal is produced at 81 gradient directions, we use 341 directions to construct the dictionary; thus, any error is due to the method's sensitivity to noise and discretization. This provides a very good starting point for the proposed constrained tractography algorithm.

In Fig. 10, we show another 40° field ($b = 3000$, noisy) but take a closer look at several points along a single fiber as it passes through the crossing region. We also examine the corresponding ODFs reconstructed using sharpened SH and the constrained approach. As expected, the sharpened SH do not detect the crossing but result in a single angle. A close examination of the reported axes shows the bias toward a single averaged axis, as reported elsewhere (23,26,39). In contrast, the proposed approach results are consistent and accurate.

In Vivo Tractography

We tested our approach on a real human brain scan acquired on a 3-T GE (Amersham, UK) system using an echo-planar imaging diffusion-weighted image sequence. A double echo option was used to reduce eddy-current related distortions. To reduce impact of echo-planar imaging spatial distortion, an eight-channel coil was used to perform parallel imaging using array spatial sensitivity encoding techniques (GE) with a SENsitivity ENcoding (SENSE)-factor (speedup) of 2. Acquisitions have 51

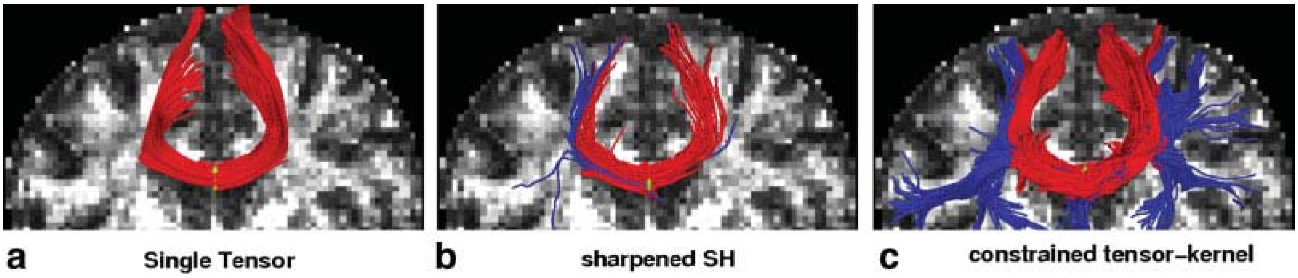

FIG. 11. Constrained tractography picks up many fiber paths consistent with the underlying structures. Both single-tensor streamline and sharpened SH are unable to find the majority of these pathways. Blue -colored fibers indicate lateral and transcallosal fibers. [Color figure can be viewed in the online issue, which is available at www.interscience.wiley.com.]

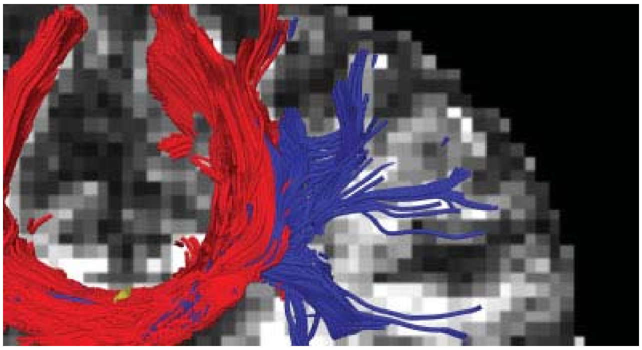

FIG. 12. Close-up of upper right in Figure 11c.

gradient directions with $b = 900$ and eight baseline scans with $b = 0$. The original GE sequence was modified to increase spatial resolution and to further minimize image artifacts. The following scan parameters were used: pulse repetition time 17,000 ms, echo time 78 ms, field of view 24 cm, 144 × 144 encoding steps, 1.7 mm slice thickness. The scan had 85 axial slices parallel to the Anterior commissure - Posterior commissure (AC-PC) line covering the whole brain.

We first focused on fibers originating in the corpus callosum. Specifically, we sought to trace out the lateral transcallosal fibers that run through the corpus callosum out to the lateral gyri. It is known that single-tensor streamline tractography only traces out the dominant pathways forming the U-shaped callosal radiation (Figs. 10a and 12a). Several studies document this phenomenon, among them, the works of Descoteaux et al. (19) and Schultz and Seidel (26) have side-by-side comparisons. These fibers have been reported using diffusion spectrum imaging (21), probabilistic tractography (12,19,40), and more recently tensor decomposition (26).

We start with two basic experiments: first, examining the tracts surrounding a single coronal slice, and second, looking at all tracts passing through the corpus callosum. We seed each algorithm multiple times in voxels at the intersection of the midsagittal plane and the corpus callosum. To explore branchings found using the proposed technique, we considered a component to be branching if it was separated from the primary component by less than 40°. Similarly, with sharpened SH, we considered it a branch if we found additional maxima over the same range. We terminated fibers when the generalized fractional anisotropy (std/rms) (14) of the estimated signal fell below 0.05.

For the first experiment, Fig. 11 shows tracts originating from within a few voxels intersecting a particular coronal slice. For a reference backdrop, we use a coronal slice showing the intensity of fractional anisotropy placed a few voxels behind the seeded coronal position. Keeping in mind that these fibers are intersecting or are in front of the image plane, this roughly shows how the fibers navigate the areas of high anisotropy (bright regions). Similar to other results (19,26), Fig. 10b shows that sharpened SH only pick up a few fibers intersecting the U-shaped callosal radiata. In contrast, our proposed method traces out many pathways consistent with the apparent anatomy. To emphasize transcallosal tracts, we color as blue those fibers exiting a corridor of ±22 mm around the midsagittal plane. Figure 12 provides a closer inspection of Fig. 7c where, to emphasize the underlying anatomy influencing the fibers, we use as a backdrop the actual coronal slice passing through the voxels used to seed this run.

For the second experiment, we seeded in all voxels of the corpus callosum lying in the midsagittal plane. Figure 13 shows the top view of the entire corpus callosum to see the overall difference between the different methods. Here again we emphasize with blue the transcallosal fibers found using all of the methods.

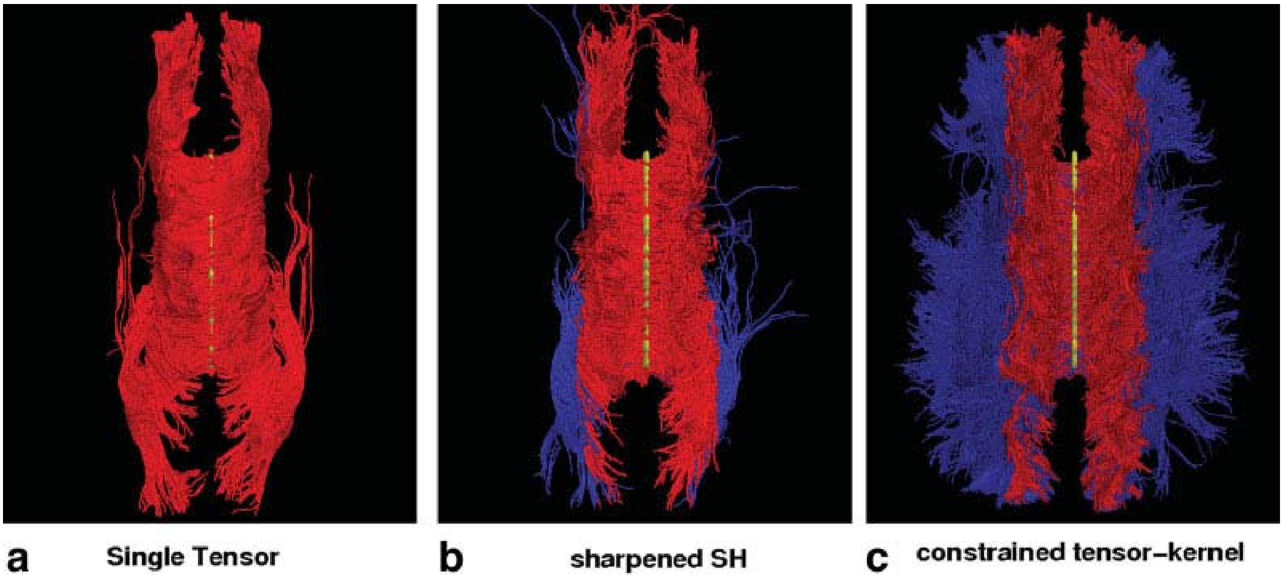

FIG. 13. Tracing fibers originating from the center of the entire corpus callosum, with the view from the top. Constrained tractography is able to find many of the lateral projections (blue), while single-tensor is unable to find any and few are found with sharpened SH. Seed region indicated in yellow.

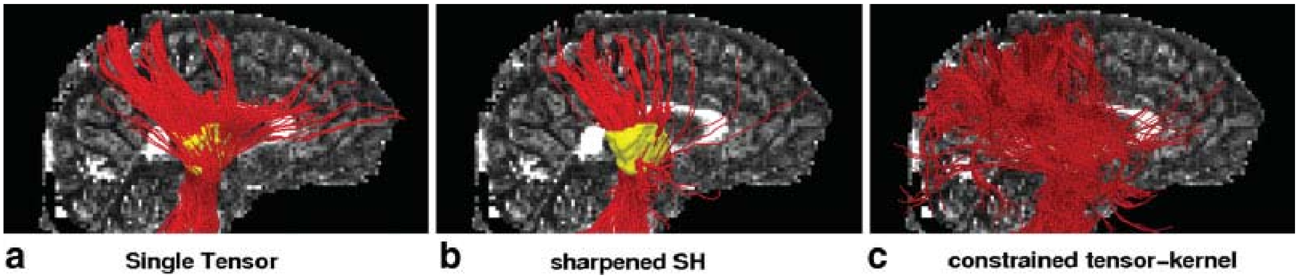

FIG. 14. Sagittal view with seeding in the internal capsule (yellow). While both single-tensor and sharpened SH tend to follow the dominant corticospinal tract to the primary motor cortex, the constrained tractography method follows many more pathways.

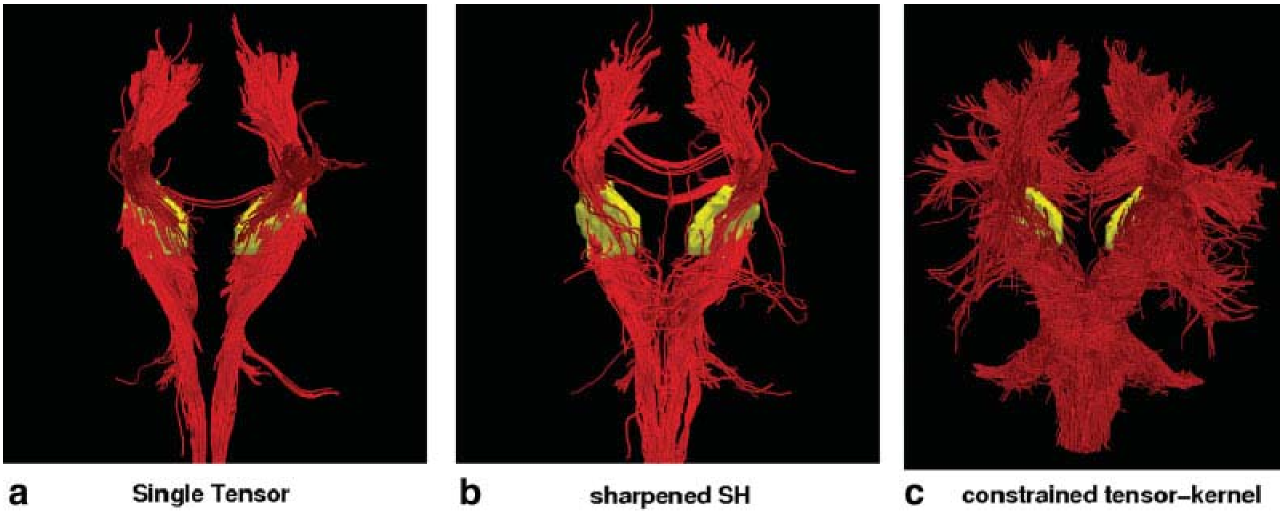

FIG. 15. Frontal view of the cortico spinal tract in each hemisphere, with seeding done in the internal capsule (yellow).

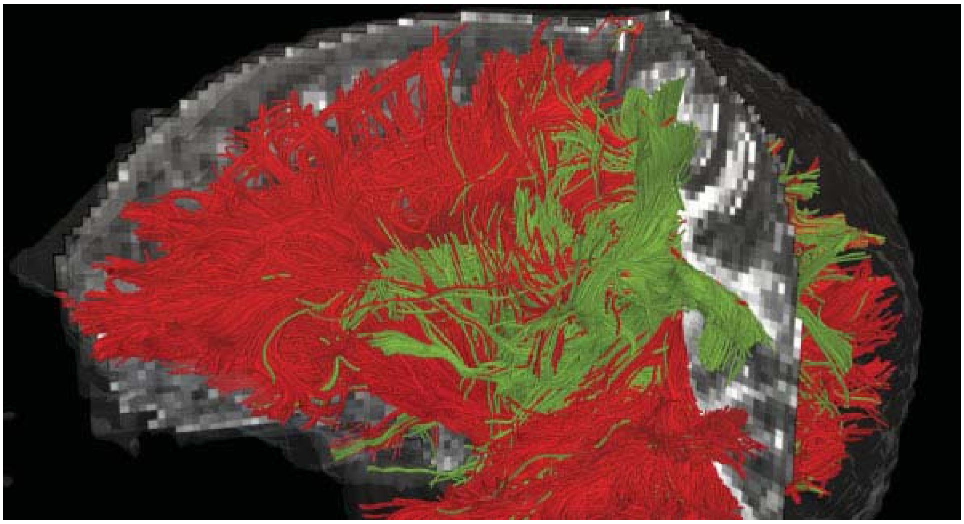

FIG. 16. Combined view of the corpus callosum (red) and corticospinal tract (green) as obtained using constrained second-order tensor kernel. Notice that different gyri are connected to the corpus callosum and corticospinal tract.

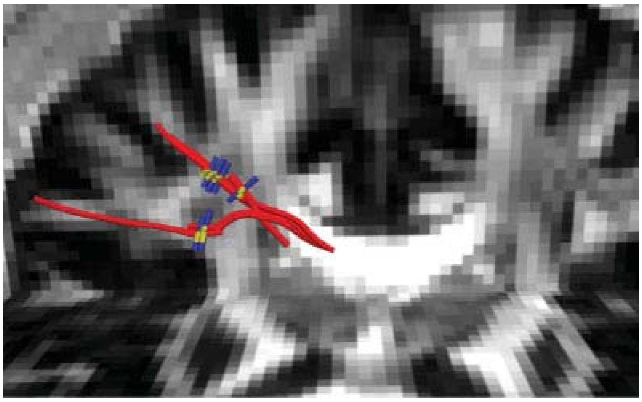

FIG. 17. Figure shows crossing of the three fiber bundles in the corona radiata. Red indicates the corpus callosum fibers, blue indicates direction of corticospinal tract, while yellow shows direction of the superior longitudinal fasciculus.

Next, we examined corticospinal tract by seeding in the internal capsule to trace out the pathways reaching up into the primary motor cortex at the top of the brain, as well as down into the hippocampal regions near the brain stem. Figure 14 shows frontal views for each technique with seeding (yellow). Figure 15 shows this same result from a side view, where we can see that the constrained approach picks up many of the corticospinal pathways, consistent with the anatomy. Figure 16 shows a combined view of the corpus callosum and corticospinal tract. Notice that the tracts corresponding to each of these pathways terminate in different regions (gyri) of the brain, consistent with the anatomy. As reported elsewhere (34), single-tensor tractography only follows the dominant corticospinal tract to the primary motor cortex. Similar pathways were also found with sharpened SH.

Next, we report results using the three-component model (Fig. 17). In this case, we seeded the midsagittal plane of the corpus callosum and traced the region known to contain three crossing bundles, namely, the the superior longitudinal fasciculus, and corticospinal tract. The proposed method picks up these three major pathways, with red showing the corpus callosum fibers, blue the direction of the corticospinal tract, and yellow the superior longitudinal fasciculus. Thus, the three-component model is able to pick up the three crossings in the in vivo data.

Note that when we use the two-component model, the region of intersection between the transcallosal fibers, the corticospinal tract, and the superior longitudinal fasciculus, leads the tractography algorithm to report several end-to-end connections that are not necessarily present, e.g., fibers originating in the left internal capsule do not pass through the corpus callosum. Many of the lateral extensions are callosal fibers that are picked up while passing through this juncture. We believe that finding such pathways is inevitable (in the absence of any a priori knowledge of the anatomy) due to poor model fitting and that they could be removed during post processing, as is typically done.

DISCUSSION

Studies involving deterministic tractography rely on the underlying model estimated at each voxel, as well as the reconstructed pathways. In this work, we demonstrated that, using a constrained estimation approach for tractography, robust estimates of much higher accuracy are obtained than independent estimation techniques. The proposed approach gives significantly lower angular error (5°) in regions with fiber crossings compared to using sharpened SH (15−20°), and it is able to reliably resolve crossings down to 25−20° compared to SH, which reaches only down to 50−60°. In vivo results on the corpus callosum and corticospinal tract demonstrate the ability of the tensor kernel in a constrained mixture model framework to find fiber tracts that are not traced using either the single tensor model or the sharpened SH approach but are nevertheless present.

Future work involves incorporating prior knowledge during tractography to avoid tracts reaching in areas that are not anatomically connected but are picked up due to partial voluming of the data. Further, we would extend this model to a mixture of three components to analyze in vivo data at $b = 3000$ or higher b-values where fiber crossings are better detected. In Eq. 6, we assumed the noise model to be gaussian, and future work involves using a Rician noise model for better estimation.

REFERENCES

1. Basser PJ, Mattiello J, LeBihan D. MR diffusion tensor spectroscopy and imaging. Biophys J 1994;66:259–267.
2. Behrens T, Woolrich M, Jenkinson M, Johansen-Berg H, Nunes R, Clare S, Matthews P, Brady J, Smith S. Characterization and propagation of uncertainty in diffusion-weighted MR imaging. Magn Reson Med 2003;50:1077–1088.
3. Alexander D, Barker G, Arridge S. Detection and modeling of non-Gaussian apparent diffusion coefficient profiles in human brain data. Magn Reson Med 2002;48:331–340.
4. Frank L. Characterization of anisotropy in high angular resolution diffusion-weighted MRI. Magn Reson Med 2002;47:1083–1099.
5. Alexander A, Hasan K, Tsuruda J, Parker D. Analysis of partial volume effects in diffusion-tensor MRI. Magn Reson Med 2001;45:770–780.
6. Tuch D, Reese T, Wiegella M, Makris N, Belliveau J, Wedeen V. High angular resolution diffusion imaging reveals intravoxel white matter fiber heterogeneity. Magn Reson Med 2002;48:577–582.
7. Kreher B, Schneider J, Mader I, Martin E, Hennig J, Il'yasov K. Multitensor approach for analysis and tracking of complex fiber configurations. Magn Reson Med 2005;54:1216–1225.
8. Friman O, Farnebäck G, Westin C-F. A Bayesian approach for stochastic white matter tractography. IEEE Trans Med Imaging 2006;25:965–978.
9. Basser PJ, Pajevic S. Spectral decomposition of a 4$^{\text{th}}$-order covariance tensor: applications to diffusion tensor MRI. Signal Processing 2007;87:220–236.
10. Barmpoutis A, Hwang MS, Howland D, Forder J, Vemuri B. Regularized positive-definite fourth order tensor field estimation from DW-MRI. Neuroimage 2009;1:153–162.
11. McGraw T, Vemuri B, Yezierski B, Mareci T. Von Mises-Fisher mixture model of the diffusion ODF. In: Int. Symp. on Biomedical Imaging, 2006. p 65–68.
12. Kaden E, Anwander A, Knsche T. Parametric spherical deconvolution: inferring anatomical connectivity using diffusion MR imaging. Neuroimage 2007;37:477–488.
13. Rathi Y, Michailovich O, Shenton M, Bouix S. Directional functions for orientation distribution estimation. Med Image Anal 2009;13:432–444.
14. Tuch D. Q-ball imaging. Magn Reson Med 2004;52:1358–1372.
15. Anderson A. Measurement of fiber orientation distributions using high angular resolution diffusion imaging. Magn Reson Med 2005;54:1194–1206.
16. Hess C, Mukherjee P, Han E, Xu D, Vigneron D. Q-ball reconstruction of multimodal fiber orientations using the spherical harmonic basis. Magn Reson Med 2006;56:104–117.
17. Descoteaux M, Angelino E, Fitzgibbons S, Deriche R. Regularized, fast, and robust analytical Q-ball imaging. Magn Reson Med 2007;58:497–510.

18. Alexander D. Multiple-fiber reconstruction algorithms for diffusion MRI. Ann Acad Sci 2005;1064:113–133.
19. Descoteaux M, Deriche R, Anwander A, Deterministic and probabilistic q-ball tractography: from diffusion to sharp fiber distributions. In: Tech. Rep 6273, INRIA Sophia Antipolis, 2007.
20. Basser P, Pajevic S, Pierpaoli C, Duda J, Aldroubi A. In vivo fiber tractography using DT-MRI data. Magn Reson Med 2000;44: 625–632.
21. Hagmann P, Reese T, Tseng W-Y, Meuli R, Thiran J-P, Wedeen VJ. Diffusion spectrum imaging tractography in complex cerebral white matter: an investigation of the centrum semiovale. In: Int. Symp. on Magnetic Resonance in Medicine, 2004. p 623.
22. Zhang F, Goodlett C, Hancock E, Gerig G. Probabilistic fiber tracking using particle filtering. In: MICCAI. 2007. p 144–152.
23. Zhan W, Yang Y. How accurately can the diffusion profiles indicate multiple fiber orientations? A study on general fiber crossings in diffusion MRI. J Magn Reson 2006;183:193–202.
24. Seunarine K, Cook P, Hall M, Embleton K, Parker G, Alexander D. Exploiting peak anisotropy for tracking through complex structures. In: MMBIA, 2007. p 1–8.
25. Bloy L, Verma R. On computing the underlying fiber directions from the diffusion orientation distribution function. In: MICCAI, 2008. p 1–8.
26. Schultz T, Seidel H. Estimating crossing fibers: a tensor decomposition approach. IEEE Trans Vis Comput Graph 2008;14:1635–1642.
27. Ramirez-Manzanares A, Cook P, Gee J. A comparison of methods for recovering intra-voxel white matter fiber architecture from clinical diffusion imaging scans. In: MICCAI, 2008. p 305–312.
28. Jian B, Vemuri B. A unified computational framework for deconvolution to reconstruct multiple fibers from diffusion weighted MRI. IEEE Trans Med Imaging 2007;26:1464–1471.
29. Jansons K, Alexander D. Persistent angular structure: new insights from diffusion MRI data. Inverse Problems 2003;19:1031–1046.
30. Tournier J-D, Calamante F, Gadian D, Connelly A. Direct estimation of the fiber orientation density function from diffusion-weighted MRI data using spherical deconvolution. Neuroimage 2004;23:1176–1185.
31. Kumar R, Barmpoutis A, Vemuri BC, Carney PR, Mareci TH. Multi-fiber reconstruction from DW-MRI using a continuous mixture of von Mises-Fisher distributions. In: MMBIA, 2008. p 1–8.
32. Tournier J-D, Yeh C, Calamante F, Cho H, Connelly A, Lin P. Resolving crossing fibres using constrained spherical deconvolution: validation using diffusion-weighted imaging phantom data. Neuroimage 2008;41:617–625.
33. Basser P, Pajevic S. A normal distribution for tensor-valued random variables: applications to diffusion tensor MRI. IEEE Trans Med Imaging 2003;22:785–794.
34. Behrens T, Johansen-Berg H, Jbabdi S, Rushworth M, Woolrich M. Probabilistic diffusion tractography with multiple fibre orientations: what can we gain? Neuroimage 2007;34:144–155.
35. Fillard VAP, Pennec X, Ayache N. Clinical DT-MRI estimation, smoothing and fiber tracking with log-euclidean metrics. IEEE Trans Med Imaging 2007;26:1472–1482.
36. Assemlal H-E, Tschumperlé D, Brun L, A variational framework for the robust estimation of odfs from high angular resolution diffusion images, In: Tech. Rep., les cahiers du GREYC, 2007.
37. Sotiropoulos S, Bai L, Morgan P, Auer D, Constantinescu C, Tench C. A regularized two-tensor model fit to low angular resolution diffusion images using basis directions. J Magn Reson Med 2008;28:199–209.
38. Mallat S, Zhang Z. Matching pursuits with time-frequency dictionaries. IEEE Trans Signal Process 1993;41:3397–2415.
39. Tournier J-D, Calamante F, Connelly A. Robust determination of the fibre orientation distribution in diffusion MRI: non-negativity constrained super-resolved spherical deconvolution. Neuroimage 2007;35:1459–1472.
40. Anwander A, Descoteaux M, Deriche R. Probabilistic Q-Ball tractography solves crossings of the callosal fibers. in: Human Brain Mapp, volume 1, 2007. p 342.